npj | quantum information

Article

Published in partnership with The University of New South Wales

https://doi.org/10.1038/s41534-026-01272-5

Mapping the positions of Two-Level-Systems on the surface of a superconducting transmon qubit

Jürgen Lisenfeld[1] ✉, Alexander K. Händel[1], Etienne Daum[1], Benedikt Berlitz[1], Alexander Bilmes[1,2] & Alexey V. Ustinov[1]

The coherence of superconducting quantum computers is severely limited by material defects that create parasitic two-level-systems (TLS). Progress is complicated by lacking understanding how TLS are created and in which parts of a qubit circuit they are most detrimental. Here, we present a method to determine the individual positions of TLS at the surface of a transmon qubit. We employ a set of on-chip gate electrodes near the qubit to generate local DC electric fields that are used to tune the TLS' resonance frequencies. The TLS position is inferred from the strengths at which TLS couple to different electrodes and comparing them to electric field simulations. We found that the majority of detectable surface-TLS was residing on the leads of the qubit's Josephson junction, despite the dominant contribution of its coplanar capacitor to electric field energy and surface area. This indicates that the TLS density is significantly enhanced near shadow-evaporated electrodes fabricated by lift-off techniques. Our method is useful to identify critical circuit regions where TLS contribute most to decoherence, and can guide improvements in qubit design and fabrication methods.

The nature of two-level tunneling systems (TLS) in amorphous materials has been puzzling generations of physicists[1]. Today, TLS are recognized as the primary source of decoherence in superconducting qubits. A type of TLS that was well-studied in glasses is thought to originate in the tunneling of a single or a few atoms between two slightly different locations in the disordered material as illustrated in Fig. 1a[2]. In superconducting circuits, amorphous surface oxides on electrodes and those used for tunnel barriers of qubit junctions are thus a known host for TLS[3–8]. In addition, microfabrication techniques were shown to spoil the crystallinity of the substrate and to leave residuals of glassy photoresist[9–11]. There is a variety of other models of TLS formation, and it remains unknown which types of TLS are limiting qubit coherence[12]. To obtain insight into the elusive microscopic TLS structure, atomistic modeling has gained in importance and was, e.g., used to characterize TLS formed by Hydrogen interstitials[13], by dangling surface atoms[14], and by tunneling atoms in Josephson junctions[15,16].

When the tunneling entity carries a charge, TLS defects possess an electric dipole moment by which they couple to the AC electric field of the resonator or qubit mode, and they quickly dissipate resonantly absorbed energy via their strong phonon coupling. Optimizing the circuit design in order to minimize the coupling of TLS to the AC-electric field from the qubit mode is thus a prerequisite for long coherence times[5,17]. The experimental progress currently relies on laborious experiments searching for better materials and improving fabrication procedures[14,17–19]. A standard method is to extract TLS loss in resonators from their power-dependent quality factor. In qubits, however, energy relaxation can be dominated by only a few of the most strongly coupled near-resonant TLS. Moreover, the resonance frequencies of TLS often fluctuate due to their electric dipole or longer-range phonon interaction with thermally activated TLS[20,21], due to diffusing charge[22], and due to the impact of high-energy particles which may redistribute the states of neighboring charge traps and bi-stable TLS[23–25]. The resulting fluctuations of qubit resonance frequencies and coherence times[26–28] are especially problematic for quantum processors as they rely on well-calibrated and stable qubits.

The strong interaction of TLS with qubits allows one to characterize them individually[3,4,29]. TLS swap spectroscopy reveals the resonance frequencies of sufficiently strongly coupled TLS by detecting minima in the qubit energy relaxation time T_1 that is measured as a function of qubit frequency[4,30,31]. This method becomes especially powerful when it is combined with means to manipulate the TLS' properties in-situ. Tuning TLS by applied mechanical strain has revealed their interactions with coherent[32] and with thermal[33] TLS, and was used to characterize the TLS' coherent dynamics[34].

Similarly, TLS were tuned by an applied DC-electric field and individually characterized with superconducting resonators[35–37]. In qubits, E-field tuning allows one to identify whether a TLS is residing in the tunnel barrier of a qubit junction[6], and provides means to enhance

[1]Physikalisches Institut, Karlsruhe Institute of Technology, Karlsruhe, Germany. [2]Google Research, Mountain View, CA, USA. ✉e-mail: juergen.lisenfeld@kit.edu

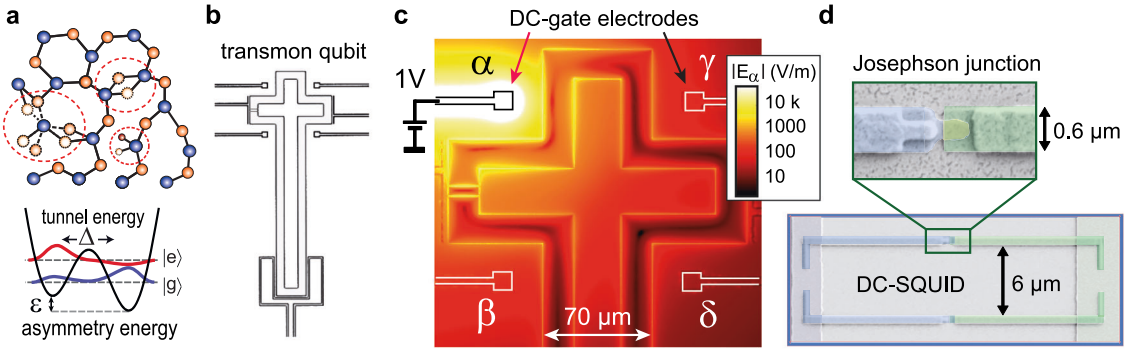

Fig. 1 | Qubit design to measure TLS locations. a Models of Two-Level-Systems (TLS) formed by delocalized atoms in an amorphous material, and corresponding TLS double-well potential that is characterized by the tunneling energy Δ between the TLS states and the asymmetry energy ε. **b** Layout of the transmon qubit, formed by a cross-shaped island that is connected via two Josephson junctions to the surrounding ground plane. **c** Four electrodes indicated by α to δ are placed around the qubit to generate locally concentrated DC-electric fields. The color encodes the simulated magnitude of the DC-electric field at the sample surface when 1V is applied to electrode α. **d** False-colored SEM picture of the DC-SQUID and a single Josephson junction.

qubit T_1 times[38,39] and their temporal stability[40]. When the tuning electric field can be spatially varied, e.g., by using two independently biased gate electrodes placed above and below the qubit chip, it is possible to obtain information on the circuit interface at which TLS reside[7]. Recently, Hegedüs et al. demonstrated scanning gate microscopy to determine the positions and electric dipole moment orientations of individual TLS at the surface of a superconducting resonator[41].

Here, we demonstrate a method to generate maps of the locations of individual TLS on the surface of a transmon qubit. The TLS locations are inferred from their measured coupling strengths to each of four on-chip gate electrodes that are placed around the qubit, realizing a method of trilateration. The majority of all detected surface-TLS were found to reside near the leads of the Josephson junctions. Considering the dominant contribution of the qubit's planar capacitor and ground plane to surface area and electric field energy, this result indicates that the TLS density is enhanced at shadow-evaporated electrodes that are deposited by additive lift-off techniques, in contrast to subtractive etching.

Results

Qubit sample with gate electrodes

The transmon qubit sample, shown in Fig. 1b–d, is based on the *XMon*-design by Barends et al.[4] and consists of a DC-SQUID and a cross-shaped island that forms a shunt capacitor with the surrounding ground plane. In addition, the design integrates four gate electrodes labeled $\alpha \ldots \delta$ in vicinity of the qubit island which are used to tune the TLS by local DC-electric fields.

The simulated E-field strength E_α when a voltage of 1V is applied to the α-electrode is shown by color in Fig. 1c. Due to the large spatial E-field gradient, the response of a TLS depends sensitively on its distance to the gate electrode. The TLS position can thus be estimated by measuring its tuning strengths to different electrodes and comparing them to the simulated strengths of the local electric fields.

TLS spectroscopy

The resonance frequency of a charged TLS is given by the hyperbolic function

$$\omega_{\mathrm{TLS}} = \sqrt{\Delta^2 + (\epsilon + 2\mathbf{p}\cdot\mathbf{E})^2}/\hbar, \tag{1}$$

where Δ is the tunneling energy between its two states, and ϵ is a background asymmetry energy of the TLS' double-well potential (see Fig. 1a) that depends on local static electric and strain fields. In addition, the asymmetry energy is tuned by the component of the applied E-field $\mathbf{E}$ at the position of the TLS that is parallel to the TLS' electric dipole moment $\mathbf{p}$. In our experiments, the E-field $\mathbf{E} = \mathbf{E}_\alpha + \mathbf{E}_\beta + \mathbf{E}_\gamma + \mathbf{E}_\delta$ is controlled via the applied voltages $V_\alpha \ldots V_\delta$ on the four gate electrodes.

We detect TLS resonances using the TLS swap-spectroscopy protocol[4,6,32] depicted in the top inset of Fig. 2a. The qubit is excited by a microwave π-pulse and tuned to one of various probe frequencies for a duration of 2.5 μs to allow for interactions with TLS. The remaining qubit excitation $P_{|1\rangle}$ then provides an estimate for the qubit T_1 time at the probe frequency[38], which shows a minimum when the qubit is in resonance with a sufficiently strongly coupled TLS.

To measure the TLS' coupling strengths to the four DC-electrodes, their resonances are traced by TLS spectroscopy while the voltages on the DC-electrodes are swept. As an example, Fig. 2a shows the resonance of a TLS that was tuned through the symmetry point of its hyperbola Eq. (1), where in each segment the voltage on the indicated gate electrode $\alpha \ldots \delta$ was stepwise increased by 1 V while other voltages were kept constant. The slope of the hyperbola in the different segments then depends on the tuning strength of the TLS by the corresponding electrode. It is obtained by fitting such traces to Eq. (1), where the factor for the induced asymmetry energy $2\mathbf{p}\cdot\mathbf{E}$ is replaced by $\sum_i \gamma_i V_i$. Here, $i \in \{\alpha, \beta, \gamma, \delta\}$ indicates the electrode that is biased by the voltage V_i, and γ_i are the fitting tuning strengths that contain information on the distance of the TLS to the corresponding electrodes.

TLS localization

Possible locations of the TLS could in principle be inferred from the measured tuning strengths by searching for positions (x,y) where the simulated electric field $\mathbf{E}_i(x,y)$ fulfills the equation $2\mathbf{p}\cdot\mathbf{E}_i(x,y,V_i) = \gamma_i V_i$. However, this would require knowledge of the TLS' electric dipole moment $\mathbf{p}$ and its orientation relative to the local E-field. In our analysis, we therefore consider only relative tuning strengths of the TLS by different electrodes, and search for positions (x,y) fullfilling the equations

$$\frac{2\mathbf{p}\cdot\mathbf{E_i}(x,y)}{2\mathbf{p}\cdot\mathbf{E_j}(x,y)} = \frac{\gamma_i V_i}{\gamma_j V_j}, \quad \text{where } \{i\neq j\} \in \alpha,\beta,\gamma,\delta. \tag{2}$$

In these equations, the TLS' electric dipole moment $\mathbf{p}$ can be eliminated given that the two fields $\mathbf{E_i}$ and $\mathbf{E_j}$ have parallel orientation at the position of the TLS. In the following, we argue that this is indeed the case in our experiment, because we are detecting only TLS in close vicinity to the edges of qubit electrodes where all electric fields are sufficiently aligned.

To be able to detect a TLS in qubit T_1-swap-spectroscopy, its (resonant) coupling strength to the qubit $g = \left(\frac{\Delta}{\hbar\omega_{\mathrm{TLS}}}\right)\mathbf{p}\cdot E_{\mathrm{rms}}$ must be large enough to result in a measurable decrease of the qubit's energy relaxation rate. Thus, TLS can only be detected in circuit regions where the qubit's AC-electric

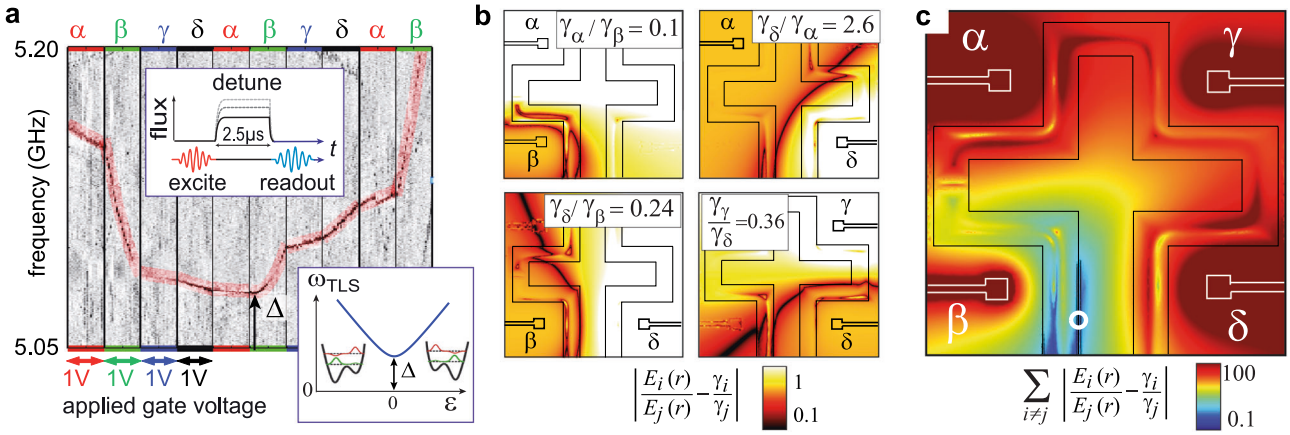

Fig. 2 | Finding the location of a TLS. a TLS spectroscopy using the protocol in the inset, to reveal the resonance frequencies of TLS from minima (dark pixels) in the resulting qubit population $P(|1\rangle)$. In each segment, the voltage on a different electrode $\alpha..\delta$ is increased by 1V. The highlighted trace shows a TLS as it is tuned through its symmetry point (arrow) according to Eq. (1) as illustrated in the lower inset. The TLS' response strengths γ_i to the different electrodes are obtained by fitting such traces to Eq. (1), and provide information about the TLS' distance to the electrodes. **b** Difference between the measured TLS response strength ratio γ_i/γ_j and the corresponding simulated E-field ratio (colorscale) for the TLS observed in **a**. Minima (dark pixels) indicate possible TLS positions. Each panel shows data from a different electrode pair as marked in the legends together with the measured tuning ratio. **c** The colorscale shows the difference sum σ (Eq. (3)) over all 6 unique combinations of electrode pairs. The minimum (white circle) marks the most probable TLS position.

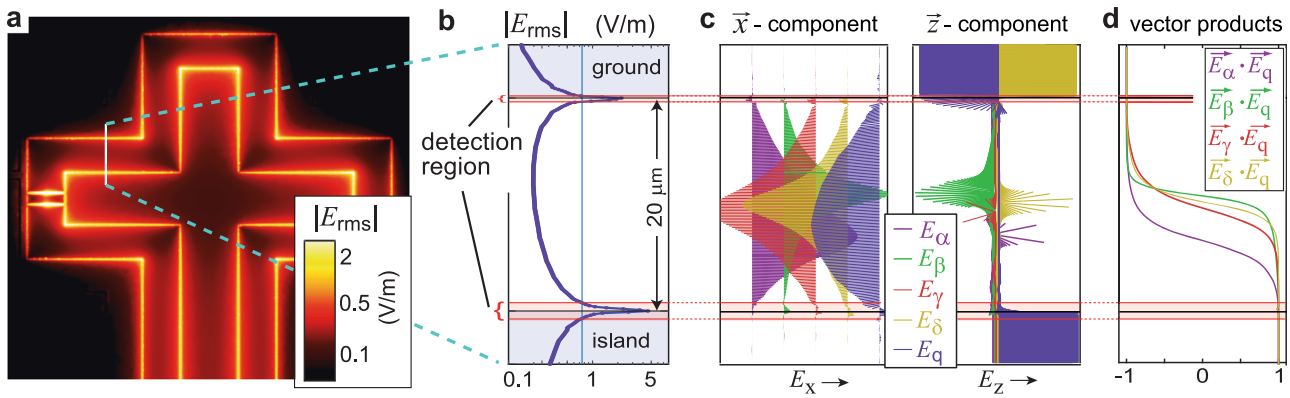

Fig. 3 | Strength and orientations of AC- and DC-electric fields. a Magnitude of the qubit's AC-electric field $|E_{\rm rms}|$ as simulated with Ansys HFSS. **b** Cross-section of $|E_{\rm rms}|$ along the white line in **a**. TLS can only be detected in the red shaded area where the field exceeds a minimum strength $E_{\rm min}$ (blue vertical line). **c** Components of the electric fields from the four electrodes and the qubit, plotted in $\vec{x}$– and $\vec{z}$ directions (left and right panel). Near the center of the gap between ground plane and qubit island, the fields induced by the gate electrodes change their direction and point in different directions. **d** The normalized vector product between the fields of gate electrodes and the qubit approaches unity near the electrode edges where all fields point in the same direction.

field strength $|E_{\rm rms}|$ exceeds $g_{\rm min}/p_\parallel$. Assuming $\Delta/\hbar\omega_{\rm TLS} \approx 1$ (most strongly coupling TLS near their symmetry point) and a field-parallel dipole moment of $p_\parallel \approx 1e$Å[3,4,36,42], the required minimum coupling strength $g_{\rm min}$ can be estimated from the energy relaxation rate of the resonantly coupled qubit-TLS system[4] $\Gamma_1 = 2\,(g_{\rm min}/\hbar)^2/\Gamma + \Gamma_{1,Q}$, where $\Gamma_{1,Q}$ is the energy relaxation rate of the isolated qubit, and $\Gamma = \Gamma_{1,\rm TLS}/2 + \Gamma_{2,\rm TLS} + \Gamma_{1,Q}/2 + \Gamma_{2,Q}$ is the sum of TLS and qubit energy relaxation and dephasing rates. The assumption that TLS are detected if they reduce the qubit's T_1 time by a factor of κ translates into a minimum coupling strength of $g_{\rm min} = \hbar\sqrt{\kappa \cdot \Gamma_{1,Q}\,\Gamma/2}$ and corresponding minimum AC-electric qubit field strength $E_{\rm min} = g_{\rm min}/p_\parallel$. A plot of these relations can be found in Supplementary Note E. For a qubit $T_1 = 7\ \mu$s, TLS coherence times in the range of $T_{1,\rm TLS} \approx T_{2,\rm TLS} \approx 0.1 - 2\ \mu$s [4,6,32,43–45], and $\kappa = 5\%$, we find a $E_{\rm min}$ range of $\approx 0.3 - 3$ V/m.

Figure 3a shows the simulated magnitude of the qubit's AC-electric field $|E_{\rm rms}|$. A cross section through the edges of ground plane and qubit island is shown in Fig. 3b and illustrates that in our qubit sample, TLS can only be detected within an $\approx 1 - 2\ \mu$m distance from the edge of qubit electrodes where $|E_{\rm rms}| > E_{\rm min}$. Since $E_{\rm min}$ decreases with the square root of the qubit's T_1 time, more coherent qubits are affected by TLS in a wider area which includes more weakly coupled ones as illustrated in Supplementary Note E.

To show that the electric fields from different on-chip electrodes are indeed sufficiently parallel, such that the dipole moment in Eq. (2) can be canceled in order to simplify the solution for possible TLS positions, in Fig. 3c we plot the electric fields' $\vec{x}$– and $\vec{z}$-components along the white line in Fig. 3a. Near the center of the gap between ground and qubit island, the E-fields point in different directions. However, within the short distance to the electrode edges where TLS are detected in our experiment, all E-fields are well aligned since their vector products with the qubit field $\vec{E}_q$ approach unity as plotted in Fig. 3d. This is also the case near the junction leads as shown in Supplementary Note E.

After dropping the TLS' electric dipole moment **p** in the vector product in Eq. (2), we find the most probable TLS position (x, y) by minimizing the sum of residuals

$$\sigma = \sum_{i\neq j} \left| \frac{E_i(x,y)}{E_j(x,y)} - \frac{\gamma_i}{\gamma_j} \right|, \quad \text{where } \{i\neq j\} \in \alpha, \beta, \gamma, \delta. \tag{3}$$

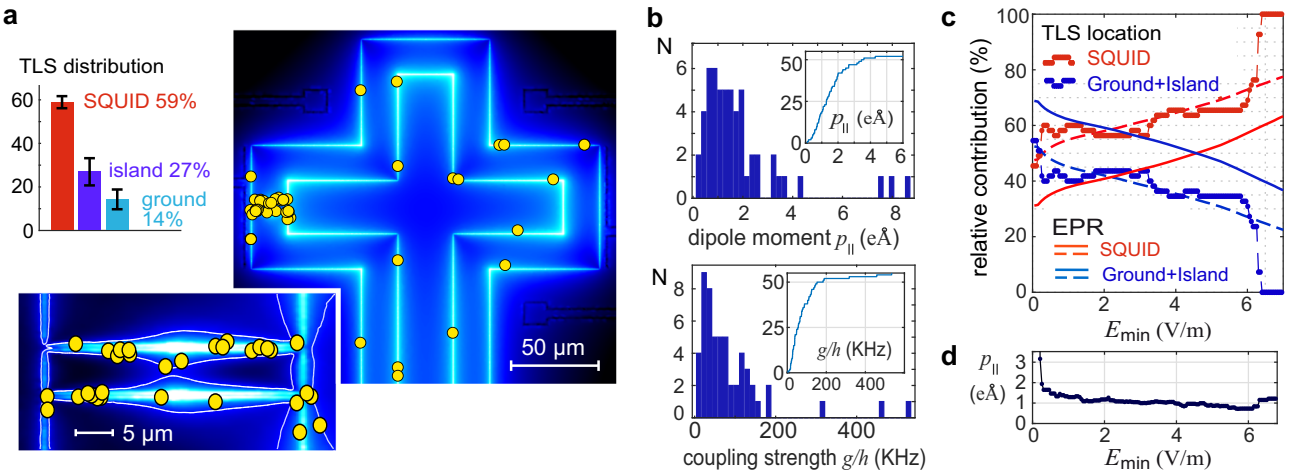

Fig. 4 | TLS locations and properties. a Map of the individual positions of detected surface-TLS (yellow circles). Most TLS (≈ 59%) were found at the Josephson junctions leads (see lower inset for a zoom on the DC-SQUID). Near the edges of capacitor island and ground plane, 27% and 14% of TLS were identified, respectively. **b** Histograms and cumulative distributions (insets) of the TLS' electric dipole moment component $p_{||}$ (upper panel) and TLS-qubit coupling strengths g/h (lower panel) as estimated from the TLS' positions, their coupling strengths to the electrodes, and the local magnitude of the qubit AC field E_{rms}. **c** Percentage of TLS identified on the SQUID vs. ground plane plus island, plotted as a function of the electric field threshold E_{min} that accounts for TLS observability in swap spectroscopy. The solid lines are the energy participation ratios (EPRs) of the SQUID (red) and the ground plus island (blue) in regions where $E_{rms} > E_{min}$. The dashed lines are a fit of these ratios to the observed TLS distribution, obtained by assuming that the TLS density in the SQUID area is enhanced by a factor of 2. **d** Determined median TLS electric dipole moment $p_{||}$ as a function of E_{min}.

Each of the six summands in Eq. (3) is the difference between the measured tuning ratio of two electrodes with the corresponding simulated E-field ratio at position (x, y). Figure 2b shows exemplarily the contribution of four summands for the TLS observed in Fig. 2a, where minima (dark pixels) indicate possible TLS positions that are confined along approximate circles centered at the electrode which is nearest to the TLS. For example, the TLS shown in Fig. 2a shows a 10 times stronger response to the β-electrode than the α-electrode. This places possible TLS positions in vicinity of the β-electrode as shown in the top left panel of Fig. 2b. Figure 2c shows a plot of the complete difference sum of Eq. (3) that contains information from all six electrode pairs, and where the global minimum (marked by a white circle) then indicates the most likely TLS position. In this analysis, we allow only solutions of TLS positions within the region where the qubit's AC field is strong enough ($|E_{rms}| > E_{min}$) so that TLS can be detected.

TLS distribution

To generate a map of the individual TLS positions on the qubit circuit, we swept the voltages on each of the four electrodes in a range between −60 V and +100 V and performed TLS spectroscopy in a 150-MHz wide window as shown in Fig. 2a. In total, 55 TLS were observed in a single qubit sample whose tuning strengths to all four electrodes could be characterized (see Supplementary Note F for further details). For the analysis, TLS were discarded whose coupling strength to the upper electrodes α and γ were indistinguishable from zero so that their location could not be precisely determined. This is the case for TLS that reside on the long arm of the qubit island (see Fig. 1b).

The determined individual TLS positions are marked by yellow circles in Fig. 4a. The majority of TLS (58%) were found to reside at the leads of the qubit's Josephson junctions. Near the edges of the qubit island and the ground plane, 25% and 16% were found, respectively. In this example, a relatively small value of $E_{min} = 0.75$ V/m was chosen as the threshold field above which TLS can be detected, which limits the area of allowed TLS positions to the thin white line in the inset of Fig. 4a.

To check the mapping procedure's reliability, the analysis is repeated for various values of E_{min}. The resulting percentages of TLS found on the SQUID leads vs. those on the qubit island and ground plane are plotted in Fig. 4c. These remain at a ratio of 60:40 within the most probable range of $E_{min} \approx 0.3..3$ V/m as estimated above, which backs the robustness of the method. Above a value of $E_{min} \approx 6$ V/m, the procedure fails since it is forced to place all TLS on the DC-SQUID. For the given data and qubit sample, we estimate an uncertainty in the TLS positions of about 6 μm as further discussed in Supplementary Note G. This resolution can be enhanced with more suitable qubit designs that avoid sharp corners.

Excess TLS density near the SQUID

Notably, the observed TLS distribution points towards an excess density of TLS near the DC-SQUID leads. Since the probability to detect a surface-TLS scales with the square of the local qubit field, the expected ratio of the numbers of TLS observed near the SQUID vs. ground plane and qubit island can be estimated by comparing their energy participation ratios (EPRs). By calculating the EPR, we limit the integrals over $|E_{rms}|^2$ to regions where $E_{rms} > E_{min}$ to account for TLS detectability in swap spectroscopy, which sets this calculation apart from the common participation ratio analysis[5] that includes also weakly coupled TLS. Further details are given in Supplementary Note E. The result is plotted with solid red and blue lines in Fig. 4c, and predicts that most TLS (>50%) would be observed on either the qubit island or ground plane in the whole range of reasonable values $E_{min} < 4$ V/m, in stark contrast to the experimental data.

This finding can be reconciled assuming that the TLS density near the DC SQUID is about two times larger than near qubit island and ground plane, presumably due to its different fabrication procedure. The expected TLS distribution for this case is shown by the dashed red and blue lines in Fig. 4c, which are obtained by scaling the electric field energy E_{rms}^2 integrated over the SQUID area by a factor of two. We find a very good agreement with the experimental result that is mostly insensitive to the choice of E_{min} in the mapping algorithm.

From the TLS' estimated positions, we can calculate their electric dipole moments using the measured tuning strengths γ_i and the simulated local E-fields of corresponding DC-gate electrodes. Similarly, the TLS' coupling strength to the qubit g can be estimated using the simulation of the qubit's AC-electric field strength at the TLS' position. Figure 4b shows their histograms and cumulative distributions for the representative example shown in Fig. 4a. The extracted median TLS dipole moment varies weakly with E_{min} as shown in Fig. 4d, and is estimated to $p_{||} \approx 1.12 \pm 0.12$ eÅ which is well in accordance with results obtained using other methods in qubits and lumped-element resonators[3,4,36].

Discussion

We have demonstrated a method to determine the individual positions and electric dipole moments of TLS defects in a transmon qubit. The majority

(≈58%) of observed strongly interfering TLS in the qubit sample were found to reside on the qubit's DC-SQUID. This confirms that the leads of tunnel junctions, due to their large electric energy participation, are a critical component which can dominate qubit loss[45–47]. This advocates for the use of wire-tapering techniques to dilute the electric field[48], and to minimize the size of lift-off structures.

Our results additionally indicate that the TLS density near the junction leads is enhanced by a factor of ≈ 2. This may be attributed to their different fabrication technique as compared to the qubit capacitor, which can promote TLS formation in various ways. For example, junction formation by shadow evaporation and electron-beam lithography is associated with larger amounts of resist residuals and enhanced roughness of junction lead interfaces[10,11,49]. The junctions were fabricated with a lift-off process which reportedly leaves excess residues[9,47]. Also, thinner films showed a larger density of grain boundaries associated with enhanced oxygen diffusion[19].

The technique to find TLS positions works with various (charge-resilient) qubit types such as flux and phase or transmon qubits, and provides information on the local TLS density in a single sample without the need to average over a large ensemble of differently designed qubits. It can be applied to arbitrary qubit designs when the grid of DC-electrodes is patterned on a wafer placed above the qubits in a flip-chip configuration. This is similar to the recently demonstrated scanning gate spectroscopy[41], but does not require mechanical control.

Control over the local DC-electric field also enables one to actively suppress decoherence by tuning dominating TLS defects out of the qubit resonance[38–40]. For this, multiple electrodes provide independent control over TLS at different locations which enhances the ability to decouple the qubit from the decohering bath.

The current method cannot determine at which interfaces TLS are residing. This is possible with additional gate electrode placed above and below the qubit chip, allowing one to also distinguish TLS located at the metal-substrate interface from those at the metal-air interface and the substrate as we showed in previous work[7]. Moreover, the combination with TLS tuning by applied mechanical strain provides additional information of TLS densities in tunnel junction barriers[6], and is useful to enhance the numbers of observable TLS in a given qubit circuit.

Our method opens door to study TLS formation due to fabrication techniques and contaminants, for example by comparing TLS densities in differently processed areas of the same qubit circuit. This approach can serve to guide improvements in qubit fabrication and design, which is vitally needed for the advancement of large-scale superconducting quantum processors where TLS defects present a major obstacle.

Methods

Sample fabrication

The qubit was fabricated from aluminum on a sapphire substrate, using optical lithography and dry etching for the ground plane and qubit island, and eBeam-patterned Dolan bridges to form the tunnel junctions and their leads (shown in Fig. 1d) in a 3-angle shadow evaporation process that avoids unwanted stray junctions[50]. Details on sample fabrication and circuit parameters are found in Supplementary Note A. The sample was cooled to a temperature of 25 - 30 mK and measured in a standard setup as detailed in Supplementary Note B.

Loss from gate electrodes

The qubit showed energy relaxation times T_1 between 5 to 8 μs at operation frequencies between 5 and 5.5 GHz. Similarly, fabricated qubits without on-chip gate electrodes achieved only slightly longer T_1-times between 10 and 20 µs[38,50], and these were mostly limited by TLS near circuit electrodes[6,51]. However, the observed T_1-time falls within the estimate range of the radiative loss via the capacitive coupling to the four electrodes, which were placed in close vicinity to the qubit island to enhance the spatial resolution in TLS localization. This loss channel can be mitigated with an improved design of the qubit and on-chip electrodes[52]. Further details on loss are discussed in Supplementary Note C.

Data availability

The raw data that support the findings of this study are available from the public repository Zenodo, DOI:10.5281/zenodo.18847452.

Received: 7 November 2025; Accepted: 7 May 2026;
Published online: 20 May 2026

References

1. Clare, C. Y. & Carruzzo, H. M. Two-level systems and the tunneling model: a critical view. *Low-Temperature Thermal and Vibrational Properties of Disordered Solids: A Half-Century of Universal Anomalies of Glasses*, 113 (2022).
2. Enss, C. & Hunklinger, S. *Low-Temperature Physics* Chap. 9 (Springer, Berlin, Heidelberg, 2005).
3. Martinis, J. M. et al. Decoherence in Josephson qubits from dielectric loss. *Phys. Rev. Lett.* **95**, 210503 (2005).
4. Barends, R. et al. Coherent Josephson qubit suitable for scalable quantum integrated circuits. *Phys. Rev. Lett.* **111,** 080502 (2013).
5. Wang, C. et al. Surface participation and dielectric loss in superconducting qubits. *Appl. Phys. Lett.* **107,** 162601 (2015).
6. Lisenfeld, J. et al. Electric field spectroscopy of material defects in transmon qubits. *npj Quantum Information* **5**, 105 (2019).
7. Bilmes, A. et al. Resolving the positions of defects in superconducting quantum bits. *Scientific Rep.* **10**, 3090 (2020).
8. De Leon, N. P. et al. Materials challenges and opportunities for quantum computing hardware. *Science* **372**, eabb2823 (2021).
9. Quintana, C. M. et al. Characterization and reduction of microfabrication-induced decoherence in superconducting quantum circuits. *Appl. Phys. Lett.* **105**, 062601 (2014).
10. Dunsworth, A. et al. Characterization and reduction of capacitive loss induced by sub-micron Josephson junction fabrication in superconducting qubits. *Appl. Phys. Lett.* **111**, 022601 (2017).
11. Gingras, M. A. et al. Improving transmon qubit performance with fluorine-based surface treatments. *arXiv preprint arXiv:2507.08089* (2025).
12. Muller, C., Cole, J. H. & Lisenfeld, J. Towards understanding two-level-systems in amorphous solids: insights from quantum circuits. *Rep. Prog. Phys.* **82**, 124501 (2019).
13. Holder, A. M., Osborn, K. D., Lobb, C. & Musgrave, C. B. Bulk and surface tunneling hydrogen defects in alumina. *Phys. Rev. Lett.* **111**, 065901 (2013).
14. Wang, Z., Yu, C. C. & Wu, R. Why superconducting ta qubits have fewer tunneling two-level systems at the vacuum-oxide interface than Nb qubits. *Phys. Rev. Appl.* **23**, 024017 (2025).
15. DuBois, T. C., Per, M. C., Russo, S. P. & Cole, J. H. Delocalized oxygen as the origin of two-level defects in Josephson junctions. *Phys. Rev. Lett.* **110**, 077002 (2013).
16. Paz, A. P., Lebedeva, I. V., Tokatly, I. V. & Rubio, A. Identification of structural motifs as tunneling two-level systems in amorphous alumina at low temperatures. *Phys. Rev. B.* **90**, 224202 (2014).
17. Ganjam, S. et al. Surpassing millisecond coherence in on chip superconducting quantum memories by optimizing materials and circuit design. *Nat. Commun.* **15**, 3687 (2024).
18. Murray, C. E. Material matters in superconducting qubits. *Mater. Sci. Eng.: R: Rep.* **146**, 100646 (2021).
19. Biznárová, J. et al. Mitigation of interfacial dielectric loss in aluminum-on-silicon superconducting qubits. *npj Quantum Inf.* **10**, 78 (2024).
20. Faoro, L. & Ioffe, L. B. Interacting tunneling model for two-level systems in amorphous materials and its predictions for their dephasing and noise in superconducting microresonators. *Phys. Rev. B.* **91**, 014201 (2015).
21. Muller, C., Lisenfeld, J., Shnirman, A. & Poletto, S. Interacting two-level defects as sources of fluctuating high-frequency noise in superconducting circuits. *Phys. Rev. B* **92**, 035442 (2015).
22. Bilmes, A. et al. Electronic decoherence of two-level systems in a Josephson junction. *Phys. Rev. B* **96**, 064504 (2017).
23. McEwen, M. et al. Resolving catastrophic error bursts from cosmic rays in large arrays of superconducting qubits. *Nat. Phys.* **18**, 107–111 (2022).

24. Thorbeck, T., Eddins, A., Lauer, I., McClure, D. T. & Carroll, M. Two-level-system dynamics in a superconducting qubit due to background ionizing radiation. *PRX Quantum* **4**, 020356 (2023).
25. Bertoldo, E. et al. Cosmic muon flux attenuation methods for superconducting qubit experiments. *New J. Phys.* **27**, 023014 (2023).
26. Klimov, P. V. et al. Fluctuations of energy-relaxation times in superconducting qubits. *Phys. Rev. Lett.* **121**, 090502 (2018).
27. Burnett, J. J. et al. Decoherence benchmarking of superconducting qubits. *npj Quantum Inf.* **5**, 54 (2019).
28. Schlör, S. et al. Correlating decoherence in transmon qubits: low frequency noise by single fluctuators. *Phys. Rev. Lett.* **123**, 190502 (2019).
29. Neeley, M. et al. Process tomography of quantum memory in a Josephson-phase qubit coupled to a two-level state. *Nat. Phys.* **4**, 523–526 (2008).
30. Osman, A. et al. Mitigation of frequency collisions in superconducting quantum processors. *Phys. Rev. Res.* **5**, 043001 (2023).
31. Colao Zanuz, D. et al. Mitigating losses of superconducting qubits strongly coupled to defect modes. *Phys. Rev. Appl.* **23**, 044054 (2025).
32. Lisenfeld, J. et al. Observation of directly interacting coherent two-level systems in an amorphous material. *Nat. Comm.* **6**, 6182 (2015).
33. Meißner, S. M., Seiler, A., Lisenfeld, J., Ustinov, A. V. & Weiss, G. Probing individual tunneling fluctuators with coherently controlled tunneling systems. *Phys. Rev. B* **97**, 180505 (2018).
34. Lisenfeld, J. et al. Decoherence spectroscopy with individual two-level tunneling defects. *Sci. Rep.* **6**, 23786 (2016).
35. Sarabi, B., Ramanayaka, A. N., Burin, A. L., Wellstood, F. C. & Osborn, K. D. Projected dipole moments of individual two-level defects extracted using circuit quantum electrodynamics. *Phys. Rev. Lett.* **116**, 167002 (2016).
36. Hung, C.-C. et al. Probing hundreds of individual quantum defects in polycrystalline and amorphous alumina. *Phys. Rev. Appl.* **17**, 034025 (2022).
37. De Graaf, S., Mahashabde, S., Kubatkin, S., Tzalenchuk, A. Y. & Danilov, A. Quantifying dynamics and interactions of individual spurious low-energy fluctuators in superconducting circuits. *Phys. Rev. B* **103**, 174103 (2021).
38. Lisenfeld, J., Bilmes, A. & Ustinov, A. V. Enhancing the coherence of superconducting quantum bits with electric fields. *npj Quantum Inf.* **9**, 8 (2023).
39. Chen, L. et al. Scalable and site-specific frequency tuning of two-level system defects in superconducting qubit arrays. *arXiv preprint arXiv:2503.04702* (2025).
40. Dane, A. et al. Performance stabilization of high-coherence superconducting qubits. *arXiv preprint arXiv:2503.12514* (2025).
41. Hegedüs, M. et al. In-situ scanning gate imaging of individual two-level material defects in live superconducting quantum circuits. *Science Advances* **11**, eadt8586 (2025).
42. Carruzzo, H. M. et al. Distribution of two-level system couplings to strain and electric fields in glasses at low temperatures. *Phys. Rev. B* **104**, 134203 (2021).
43. Shalibo, Y. et al. Lifetime and coherence of two-level defects in a Josephson junction. *Phys. Rev. Lett.* **105**, 177001 (2010).
44. Chen, M., Owens, J. C., Putterman, H., Sch afer, M. & Painter, O. Phonon engineering of atomic-scale defects in superconducting quantum circuits. *Sci. Adv.* **10**, eado6240 (2024).
45. Weeden, S. et al. Statistics of strongly coupled defects in superconducting qubits. *Phys. Rev. Appl.* **25**, 044050 (2026).
46. Deng, H. et al. Titanium nitride film on sapphire substrate with low dielectric loss for superconducting qubits. *Phys. Rev. Appl.* **19**, 024013 (2023).
47. Smirnov, N. S., Krivko, E. A., Solovyova, A. A., Ivanov, A. I. & Rodionov, I. A. Wiring surface loss of a superconducting transmon qubit. *Sci. Rep.* **14**, 7326 (2024).
48. Martinis, J. M. Surface loss calculations and design of a superconducting transmon qubit with tapered wiring. *npj Quantum Inf.* **8**, 26 (2022).
49. Moskalev, D. O. et al. Optimization of shadow evaporation and oxidation for reproducible quantum Josephson junction circuits. *Sci. Rep.* **13**, 4174 (2023).
50. Bilmes, A., Händel, A. K., Volosheniuk, S., Ustinov, A. V. & Lisenfeld, J. In-situ bandaged Josephson junctions for superconducting quantum processors. *Superconductor Sci. Technol.* **34**, 125011 (2021).
51. Daum, E., Berlitz, B., Deck, S., Ustinov, A. V. & Lisenfeld, J. Investigation of parasitic two-level systems in merged-element transmon qubits. *arXiv preprint arXiv:2509.22593* (2025).
52. Bilmes, A., Volosheniuk, S., Brehm, J. D., Ustinov, A. V. & Lisenfeld, J. Quantum sensors for microscopic tunneling systems. *npj Quantum Inf.* **7**, 27 (2021).

Acknowledgements

We thank Hannes Rotzinger for his support with the experimental setup and fruitful discussions, and Lukas Radtke for his commitment to the clean-room and help with sample fabrication.

Author contributions

J.L. conceived and supervised the project and wrote the manuscript. E-field tuning techniques were developed by J.L. and A.B. Data was acquired and analyzed by J.L. with support from A.K.H. and B.B. The sample was fabricated by A.K.H. and A.B. Simulations were done by A.K.H., E.D, and B.B. The experimental infrastructure was provided by A.V.U. All authors contributed to discussion and the final manuscript.

Funding

Open Access funding enabled and organized by Projekt DEAL.

Competing interests

The authors declare no competing interests.

Additional information

Supplementary information The online version contains supplementary material available at https://doi.org/10.1038/s41534-026-01272-5.

Correspondence and requests for materials should be addressed to Jürgen Lisenfeld.